Insight into phase stability and thermoelectric properties of semiconducting iron silicides with manganese substitution: β-Fe$_{1-x}$Mn$_x$Si$_2$ (0≤x≤0.05)

Sopheap Sam [a], Umar Farooq [b], Rio Oshita [b], Hiroshi Nakatsugawa [b,*]

[a] National Institute for Materials Science, Tsukuba, Ibaraki, 305-0044, Japan
[b] Yokohama National University, Yokohama, 240-8501, Japan

ARTICLE INFO

ABSTRACT

Metal-doped iron silicides (β-FeSi$_2$) are promising thermoelectric materials for high-temperature applications. However, the addition of metal dopants usually causes the formation of secondary metallic phases, resulting in the degradation of thermopower. Here we report the stability of semiconducting β-phase (higher than 95 %) of Mn-doped β-FeSi$_2$ obtained at Mn concentration from 1 % to 5 %, where the samples were prepared through direct arc melting and heat treatment process. The carrier density remarkably increases with Mn content, but the mobility decreases. The electrical resistivity significantly decreases with Mn content. The Seebeck coefficient of Mn-doped samples is improved and stable at high-temperature regions because of the reduction of the bipolar effect and β-phase stability. The thermal conductivity slightly increases with Mn. As a result, the maximum thermoelectric power factor $PF = 970$ μWm^{-1}K^{-2} and dimensionless figure of merit $ZT = 0.12$ at 800 K are obtained in a 3 % Mn-doped sample. The stability of β-phase and the improved carrier density are the origins of enhanced thermoelectric properties, where the Seebeck coefficient is improved, and the electrical resistivity is reduced. Our study provides insight into the importance of phase stability for enhancing thermoelectric transport in Mn-doped β-FeSi$_2$.

1. Introduction

Thermoelectric (TE) devices have gained interest in various applications such as waste heat recovery, refrigeration, and biomedical applications. In waste heat recovery, the TE generator could directly convert it into electricity without any moving parts and no gas or mechanical pollution to the environment [1,2]. The TE generator has been also used to recover energy loss from the exhaust heat generated by the vehicles [3,4]. In cooling applications, a TE cooler is used to cool down the electronic hot spot to increase the lifespan of electronic devices [5]. In biomedical applications, it was reported that the TE device could effectively accelerate the wound-healing process faster than natural healing [6]. The efficiency of TE devices is mainly dependent on the performance of TE materials. The TE material performance is defined by the dimensionless figure of merit (ZT) as expressed by Ref. [7]:

$$ZT = S^2 \rho^{-1} \kappa^{-1} T \tag{1}$$

Where S is the Seebeck coefficient, T is temperature, ρ is electrical resistivity, and κ is thermal conductivity dominated by the electronic and

lattice part ($\kappa = \kappa_e + \kappa_l$). Usually, the part $S^2\rho^{-1}$ in Equation (1) is called the power factor (PF) of the materials. Traditional TE materials such as Pb and Bi-based compounds [8–10] are high-cost and toxic. Thus, many studies are trying to improve the properties of abundant and non-toxic materials such as oxides [11–15], sulfides [16–18], intermetallic Heusler [19–21], and silicide-based compounds [22–31]. Among silicide alloys, the semiconducting iron silicide (β-FeSi$_2$) has gained attention for high-temperature TE applications due to its thermal stability and strong oxidation resistance [32,33]. However, the TE performance of pristine β-FeSi$_2$ was not good enough due to the high ρ and decrease of the $|S|$ at high temperatures due to the contribution of the bipolar effect, leading to the reduction in PF values. By increasing the carrier concentration (n_H) of β-FeSi$_2$, the ρ can be decreased and the $|S|$ value can be improved simultaneously, resulting in the improvement of PF values. The increase in n_H can be effectively obtained by the addition of dopants. However, adding dopants causes the formation of the secondary phases (metallic phases) [30,34–36] which is not preferable in TE application because the S value of metallic materials is very small ($S = -\Delta V/\Delta T$) compared to semiconducting materials. Therefore, to decrease the ρ while maintaining the S, the suppression of the secondary metallic phases is

required in the β-FeSi$_2$ system.

Recently, Qiu et al. reported the highest *ZT* of 0.6 at 1000 K obtained in 16 % Ir-doped β-FeSi$_2$ prepared by spark plasma sintering (SPS) method [27]. It was found that Ir element could not only improve *PF* value but also decrease κ, where its role is a heavy element for phonon scattering. Cheng et al. reported that the maximum *ZT* of 0.3 at 900 K was obtained in an 8 % Co-doped β-FeSi$_2$ by applying a long heat treatment process for 15 days [30]. In addition, Le tonquesse et al. obtained a 20 % reduction in κ due to stacking fault structure in a 7 % Co-doped β-FeSi$_2$ sample prepared by the magnesioreduction synthesis technique. As a result, the maximum *ZT* of 0.18 was obtained at 773K. Dabrowski et al. reported a maximum *ZT* of 0.15 obtained in a 3 % Co-doped β-FeSi$_2$ sample prepared by pulse plasma sintering method [34]. They found that the ε-phase was formed with the addition of Co and Mn. To obtain p-type β-FeSi$_2$, doping with Al is also effective for improving the transport properties. Chen et al. reported that the electrical conductivity and Seebeck coefficient of β-FeSi$_2$ were simultaneously improved by Al doping, resulting in a maximum *ZT* of 0.11 at 5 % Al addition [37]. Du et al. investigated the thermoelectric properties of p-type FeSi$_{2-x}$Al$_x$ fabricated by the SPS method. They reported the highest *ZT* = 0.18 at 850 K was obtained in *x* = 0.04 [38]. This was because when *x* > 0.04, the formation of secondary phases occurred, causing the deterioration |*S*|. By alloying with the Os element, the *ZT* was further improved up to 0.35 due to the remarkable reduction in κ. In addition, it was reported that the *ZT* of β-FeSi$_2$ was enhanced up to 0.31 at optimum doping levels of 3 % Co + 1 % Ni [39]. However, the secondary phases increase with Co and Ni doping [40]. Zhao et al. investigated the effect of Si content on the TE properties of Mn-doped FeSi$_x$ prepared by the hot-pressing method. The ε-phase was formed when *x* ≤ 1.9; therefore, the highest *ZT* of 0.17 at 873 K was obtained in the *x* = 2 sample [41]. Based on a series of previous reports, the formation of secondary phases is sensitive to the TE performance. Therefore, it has been a challenge to maintain the semiconducting β-phase when the dopant is introduced to the β-FeSi$_2$. In addition, the key point is what we could achieve when the β-phase is stabilized even though the dopant is introduced to the β-FeSi$_2$. Importantly, the correlation between the phase contents and transport properties needs to be further discussed in depth.

In this work, we comprehensively investigate the structure evolutions, phase contents, electrical conduction, and transport properties of Fe$_{1-x}$Mn$_x$Si$_2$ (0 ≤ *x* ≤ 0.05) fabricated by direct arc melting and heat treatment process. Since we aim to study the TE properties of p-type β-FeSi$_2$-based materials, the Mn element is chosen as a dopant to tune the conduction of β-FeSi$_2$ from n-type to p-type semiconductors. The TE properties are investigated from 80 K to 800 K and the relationship between the phase contents and transport properties is also discussed. In addition, we found that the addition of Mn up to *x* = 0.05 could maintain the semiconducting β-phase higher than 95 % which is beneficial for TE transport.

2. Experiments

The raw materials of Fe grain (99.9 % up), Mn grain (99.9 % up), and Si grain (99.999 %) were weighted for a total mass of 20g for each compositional ratio of Fe$_{1-x}$Mn$_x$Si$_2$ where (0 ≤ *x* ≤ 0.05). The mixtures of raw materials were melted using an arc melting apparatus in an argon atmosphere under a vacuum pressure of 10^{-3} Pa. To ensure homogeneity, the ingots were flipped and remelted three times. The ingots were sliced into the appropriate pieces (size: 7mm × 7mm × 1.5 mm for the characterization of transport properties) using a numerical control wire-cutting machine (Makino, EC-3025). The obtained ingots from arc melting are in metallic phases (α-Fe$_2$Si$_5$ and ε-FeSi); therefore, the heat treatment was applied to transform them into a semiconducting phase (β-FeSi$_2$). The samples were heat-treated at 1423 K for 3 h and followed by 1113 K for 20 h in a vacuum-sealed silica quartz ampule. The first step of heat treatment was to further homogenize materials distribution

and the second step was to transform the metallic phase into the semiconductor phase. The heat treatment process followed the previous report [42], where the conditions were optimized.

The powder X-ray diffraction (XRD) measurement was performed using an X-ray diffractometer (SmartLab, RIGAKU) equipped with Cu K-α having a wavelength of 1.5418 Å. The obtained XRD data were used for the calculation of crystal structure parameters and phase identification employing the Rietveld refinement method in the RIETAN-FP program. The Fe1 and Fe2 occupancy was set to *x* while that of Mn1 and Mn2 were set to 1-*x* for 0 ≤ *x* ≤ 0.05. The standard crystal data were taken from the Inorganic Crystal Structure Database (ICSD). The code 9119-ICSD [43] was used for β-phase, code 41997-ICSD [44] is for ε-phase, and code 5257-ICSD [45] is for α-phase. The microstructures were observed by the scanning electron microscope (SEM, VE-8800, KEYENCE). The density of sample was measured by Archimedes method. The electrical properties such as carrier density (n_H) and mobility ($μ_H$) were measured at room temperature using the ResTest8300 apparatus (TOYO Co.). The thermoelectric properties such as resistivity (ρ) and Seebeck coefficient (*S*) were measured from 80 K to 800 K using ResiTest8300 and home-built apparatus. The thermal conductivity (κ) was characterized using the power efficiency measurement system (PEM2, ULVAC, Inc).

3. Results and discussion

3.1. Structure and phase analysis

The XRD patterns and microstructures of FeSi$_2$ are illustrated in Fig. 1. The arc-melted sample (before heat treatment) is crystallized in metallic phases (ε-FeSi + α-Fe$_2$Si$_5$) as confirmed at all indexed peaks of the XRD patterns (Fig. 1 (a)). In addition, the inset shows the surface morphology with the grain of ε-phase (bright grain) and α-phase (dark grain). This tendency is similar to the previous report of Dabrowski et al. [34]. The pores are also formed due to the fast cooling of the copper hearth. After the heat treatment, the XRD patterns indicate that the sample is crystallized in the semiconducting phase (β-FeSi$_2$) confirmed by the indexed peaks (Fig. 1 (b)). The trace of ε-phase at 2θ = 45.2° was also observed at the right side of the indexed peak 421. As shown in the inset, the surface morphology is homogenous, indicating that only β-phase is formed after heat treatment. Therefore, this suggests that heat treatment is very important in the process of transforming metallic phases into a semiconducting phase for the iron-silicide system. Interestingly, the size of pores is enlarged compared to that before heat treatment. The behavior occurred during the heat treatment process when the volume of β-phase was transformed from ε and α-phase (β-FeSi$_2$ ← ε-FeSi + α-Fe$_2$Si$_5$). The pores usually contribute to the reduction in lattice thermal conductivity, where phonons are scattered more frequently compared to a system with less pores. However, the relative densities of our samples (0 ≤ *x* ≤ 0.05) are higher than 95 % (Table 1). Based on such high-density samples, the formation of pores should have no significant influence on the analysis of thermoelectric properties.

Fig. 2 shows the Rietveld refinement results for Fe$_{1-x}$Mn$_x$Si$_2$ (0 ≤ *x* ≤ 0.05), where black, red, blue, green, and pink lines represent the experimental data, β-phase, ε-phase, α-phase, and the difference between the data respectively. In Table 1, the reliability factor of the weighted diffraction pattern R_{wp} is 2.9 % < R_{wp} < 3.4 %, and the index *S* = R_{wp}/R_e representing a comparison with R_e corresponding to the statistically expected minimum R_{wp} is 1.3 < *S* < 4.1. This indicates that goodness of fitting is obtained, suggesting that the samples are grown in β-phase. The small peak of the ε-phase was observed as magnified in the inset or pointed out by the arrow. The amount of phase content will be discussed in the next part. Regarding the lattice parameters, it is found that the volumes (*V*) of Mn-doped samples range from 606 Å^3 to 609 Å^3 which are slightly bigger than that of the non-doped sample (*V*~605 Å^3) (Table 1). This is because Mn has a larger atomic radius (r_{Mn} = 1.39 Å)
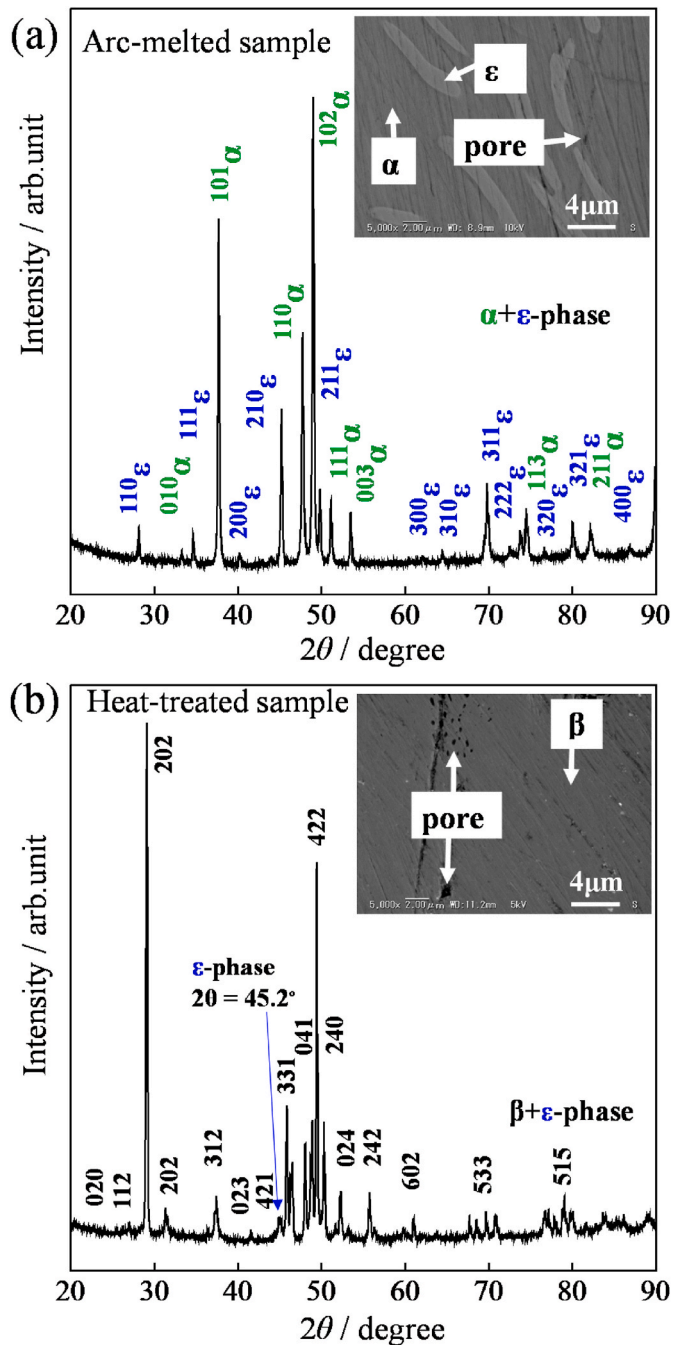
Fig. 1. XRD patterns of FeSi$_2$ (a) arc-melted sample before heat treatment having the peaks of metallic ε and α-phase and (b) heat-treated sample having the peaks of semiconducting β-phase with a trace of ε-phase at the right side of indexed peak 421 as pointed out by the arrow. The inset shows the microstructures of each sample.

Table 1
Lattice parameters, reliability factor, relative density, and phase occupations were calculated by Rietveld analysis for Fe$_{1-x}$Mn$_x$Si$_2$ ($0 \leq x \leq 0.05$).

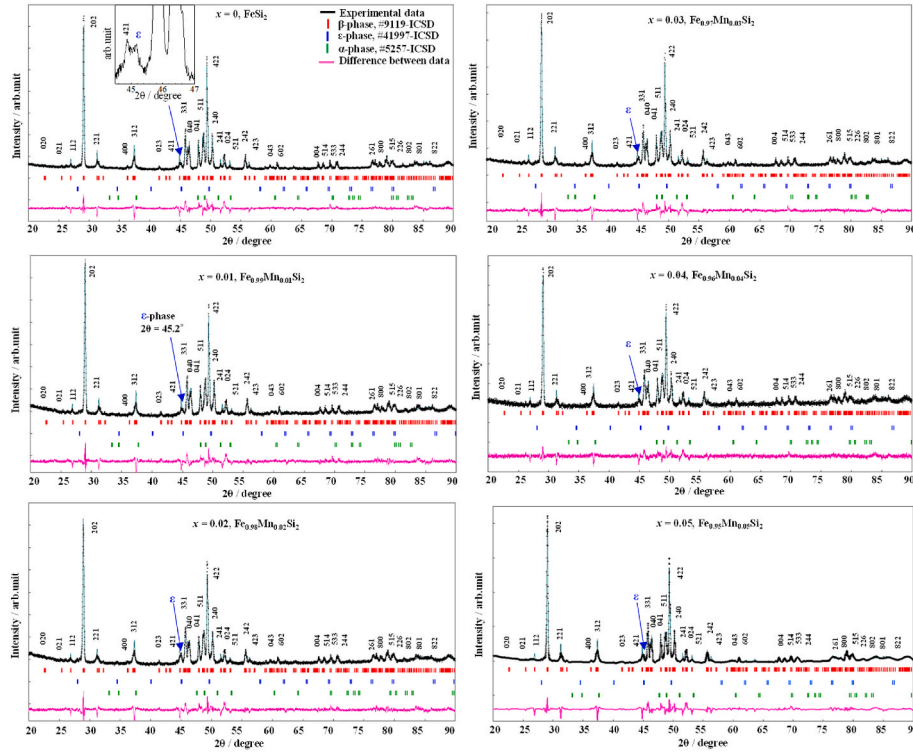| Samples	Fe$_{1-x}$Mn$_x$Si$_2$					
Composition, *x*	0	0.01	0.02	0.03	0.04	0.05
Space group	*Cmce*	*Cmce*	*Cmce*	*Cmce*	*Cmce*	*Cmce*
Lattice parameters						
a (Å)	9.8868	9.9008	9.9061	9.8882	9.8863	9.8878
	(2)	(2)	(3)	(2)	(2)	(2)
b (Å)	7.8068	7.8214	7.8272	7.8136	7.8129	7.8154
	(1)	(2)	(2)	(1)	(2)	(1)
c (Å)	7.8436	7.8579	7.8658	7.8514	7.8509	7.8542
	(2)	(2)	(3)	(2)	(3)	(2)
V (Å^3)	605.41	608.5	609.90	606.62	606.21	606.95
	(2)	(2)	(3)	(2)	(2)	(2)
Reliability factor						
R_{wp} (%)	3.251	3.038	2.950	3.012	3.475	2.922
R_e (%)	0.792	1.559	1.575	0.815	1.549	2.160
$S = R_{wp}/R_e$	4.105	1.949	1.873	3.696	2.243	1.353
Relative density (%)	98.0(1)	97.0(3)	98.1(3)	97.6(5)	95.4(3)	96.4(3)
Phase occupation						
β-phase (%)	97.52	96.45	96.49	96.52	97.95	97.35
ε-phase (%)	1.41	0.98	2.18	1.60	0.60	1.63
α-phase (%)	1.07	2.57	1.32	1.88	1.45	1.02

amount of β-phase decreases (lower than 95 %) with increasing doping level (*x*) from 0 to 0.05. Therefore, the Mn-doped samples have better phase stability. It should be noted that the decrease in semiconducting β-phase or increase in metallic ε + α-phases deteriorates the thermopower and increases thermal conductivity, leading to a decline in TE performance.

3.2. Electrical transport

The carrier density (n_H) and mobility (μ_H) at room temperature of Fe$_{1-x}$Mn$_x$Si$_2$ ($0 \leq x \leq 0.05$) is listed in Table 2 and plotted in Fig. 4. The n_H remarkably increases from $\sim 10^{16}$ cm^{-3} to $\sim 10^{18}$-10^{19} cm^{-3} as *x* increases from 0 to 0.05, respectively. In Table 2, the sign of the Seebeck coefficient (*S*) for *x* = 0 is negative (−), indicating an n-type semiconductor. The sign of *S* changes to positive (+) for $0.01 \leq x \leq 0.05$, indicating a p-type semiconductor. This tendency suggests that Mn is an acceptor for β-FeSi$_2$, and it tunes the conduction properties from n-type to p-type, where the hole concentration increases with Mn substitutions. The n_H values of our samples (*x* = 0.01, $n_H = 2.4(3) \times 10^{18}$ cm^{-3} and *x* = 0.03, $n_H = 6.1(5) \times 10^{18}$ cm^{-3}) prepared by the direct arc melting method are slightly higher than the previous report (*x* = 0.01, $n_H = 8.9 \times 10^{17}$ cm^{-3} and *x* = 0.03, $n_H = 2.9 \times 10^{18}$ cm^{-3}) prepared by cold pressing and sintering method [46]. This is probably because the relative density of our samples (>95 %, Table 1) is higher than cold pressing and sintering samples (80 %). The increase in n_H contributes to the improvement in both electrical conductivity and the Seebeck coefficient due to the reduction in the bipolar effect [47], leading to an improvement in the power factor of TE materials. However, it should be noted that the β-phase also has an important role in maintaining the Seebeck coefficient. For β-FeSi$_2$, the formation of metallic ε and α-phases is so sensitive to the dopant. If the metallic phases increase with the doping level, the Seebeck coefficient will remarkably decrease [28,39]. Therefore, the increased n_H and β-phase stability are required to enhance the TE properties of iron silicide.

Fig. 4 also shows the mobility (μ_H) decreases with *x*. The μ_H decreases from 37(4) cm^{2}V^{-1}s^{-1} to 5.6(9) – 3.3(8) as *x* increases from 0 to 0.05, respectively (Table 2). The decrease in μ_H with increasing Mn doping has a similar tendency when Co [26,48,49] and Ni [28,48] are doped with β-FeSi$_2$. This is due to the increased scattering frequency when the carrier density improved by adding dopants. The decreased μ_H has a

than that of Fe ($r_{Fe} = 1.25$ Å). Similarly, the previous report also pointed out that the lattice volume becomes bigger when dopants Ru [36] and Co [26] are introduced to the host β-FeSi$_2$ because the radius of Ru and Co are larger than Fe.

To quantitatively evaluate the phase contents, we performed the Rietveld refinement, and the results are plotted in Fig. 3. For all samples, the β-phase occupies more than 95 % (Fig. 3 (a) and Table 1). Other than β-phase, the secondary metallic ε + α-phases share the occupation with just less than 5 %. This tendency suggests that dopant Mn is well soluble in β-FeSi$_2$, contributing to improvement in thermopower. As shown in Fig. 3 (b), if we compare it to other dopants such as Co and Ni [40], the

Fig. 2. Rietveld refinement result of $Fe_{1-x}Mn_xSi_2$ ($0 \leq x \leq 0.05$) after the heat treatment. The black curve is experimental data, red is β-phase, blue is ε-phase, green is α-phase, and pink is the difference between the data. All samples crystalize in semiconducting β-phase with the trace of ε-phase at $2\theta = 45.2°$ as magnified in the inset and pointed out with the arrow.

negative impact on electrical conductivity; however, the increased n_H contributes to enhancing it. In addition, the large decrease in carrier mobility with a low amount of Mn doping is due to the increase in effective mass, and almost unchanged with a high amount of Mn doping because the effective mass is almost constant. This point will be clarified in the next section on the relationship between the Seebeck coefficient and carrier density.

The temperature-dependent electrical resistivity (ρ) for $Fe_{1-x}Mn_xSi_2$ ($0 \leq x \leq 0.05$) is illustrated in Fig. 5 (a). The ρ of all samples decreases with increasing temperature, indicating the semiconducting behavior from 80K to 800K. In addition, the ρ of all Mn-doped samples($0.01 \leq x \leq 0.05$) are remarkably lower than that of the non-doped sample ($x = 0$). The decrease in ρ with Mn content is due to the increased n_H as discussed above. This relationship can be explained by Ref. [50]:

$$\rho = |e|^{-1}\mu_H^{-1}n_H^{-1} \tag{2}$$

Where ρ, e, μ_H, and n_H are resistivity, elementary charge, mobility, and carrier density, respectively. Equation (2) implies that ρ is inversely proportional to n_H. As a result, the increased n_H in Mn-doped samples contributes to the reduction in ρ, enhancing TE performance.

We then estimate the activation energy (E_a) using the data of ρ with temperature dependence as a function of n_H and μ_H. At high temperatures, the relationship between n_H and T is expressed by Ref. [51]:

$$n_H \propto T^{3/4}\exp\left(\frac{-E_a}{2k_BT}\right) \tag{3}$$

Where k_B is the Boltzmann constant. When the impurity is introduced to the host material, the proportionality between μ_H and T is expressed by Ref. [52]:

$$\mu_H \propto T^{3/2} \tag{4}$$

By substituting Equations (3 and 4) into (2), the relation of ρ with E_a can be defined as follows:

$$\rho T^{9/4} \propto \exp\left(\frac{E_a}{2k_BT}\right)$$

$$\Leftrightarrow \ln\left(\rho T^{9/4}\right) \propto \frac{E_a}{2k_BT} = \frac{E_a}{2000k_B}1000T^{-1} \tag{5}$$

By using Equation (5), we make the Arrhenius plot of $\ln(\rho T^{9/4})$ versus $1000T^{-1}$ as shown in Fig. 5 (b) and the values of E_a can be evaluated from the slope of the straight lines, where the slope is equal to $E_a/(2000k_B)$. The E_a of intrinsic $x = 0$ is about 0.524 eV, closing to the band gap value ($\sim$0.7eV) reported by Clark et al. [53]. Equation (3) implies that the activation energy (E_a) depends on the thermal activation process of the carrier density, indicating that E_a is very much related to the band gap. In addition, the E_a values decrease with increasing x, suggesting that the addition of Mn moves the Fermi level closer to the valence band. Therefore, the electrons require a lower energy to excite from the valence band to the acceptor level. The E_a of our samples ($x = 0.01$, $E_a = 0.132$ eV, and $x = 0.03$ $E_a = 0.108$ eV) are about one-third of an order of magnitude smaller than the previous report of Tani et al. ($x = 0.01$, $E_a = 0.299$ eV and $x = 0.03$ $E_a = 0.258$eV) [46]. The smaller E_a values of our samples should be due to the higher n_H as discussed above. In addition, based on the density functional theory reported by Sen et al. [54], the Fermi level moves near the valence band with increasing Mn doping. This tendency is consistent with our experimental results, where Mn acts as an acceptor, and the carrier density increases with increasing Mn doping levels. Moreover, the movement of the Fermi level close to the valence band also agrees with the result of the activation energy, where the activation energy decreases with Mn doping.

3.3. Thermoelectric properties

Fig. 6 illustrates the temperature-dependent Seebeck coefficient (S) for $Fe_{1-x}Mn_xSi_2$ ($0 \leq x \leq 0.05$) and Pisarenko's plot of $|S|$ versus n_H. As shown in Fig. 6 (a), the $|S|$ of the $x = 0$ sample increases as temperature
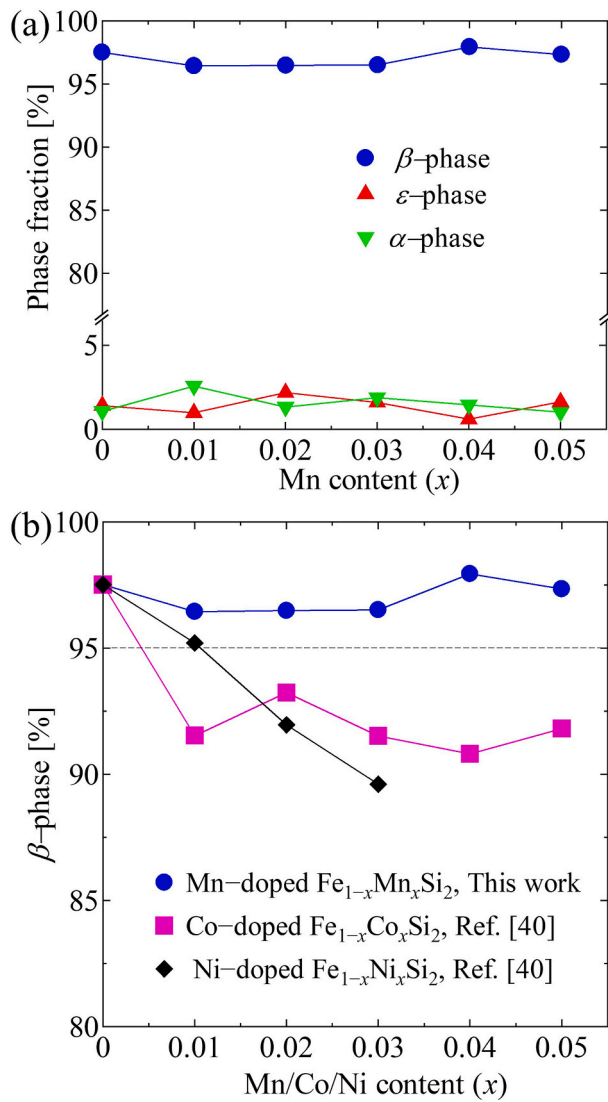
Fig. 3. (a) Mn dependence of phase fraction in Fe$_{1-x}$Mn$_x$Si$_2$ ($0 \leq x \leq 0.05$). The semiconducting β-phase occupies more than 95 % while the metallic ε and α-phases occupy less than 5 %. (b) comparison of the β-phase content of Mn-doped samples in this work with Co and Ni-doped samples in the previous report in Ref. [40]. When doping (x) increases from 0 to 0.05, the amount of β-phase in Co and Ni-doped samples decreases to less than 95 % while that of Mn-doped samples maintains higher than 95 %.

increases from 80 K to 420 K due to the transition from impurity band conduction to polaron conduction [55]. It then turns to decrease as temperature increases from ~290 μVK^{-1} to 0 μVK^{-1} as temperature increases from 420 K to 800 K. The decrease in $|S|$ of the $x = 0$ sample at high temperature is caused by the bipolar effect that usually occurs in intrinsic semiconducting materials with low n_H [47,56]. Compared to

the previous reports at room temperature, our $x = 0$ sample exhibits an n-type semiconductor which is in agreement with the previous reports of Cheng et al. [30] and Du et al. [38]. In contrast, Ito et al. [57,58] reported that the conduction of the $x = 0$ sample exhibited a p-type material. The difference in the conduction type of the $x = 0$ sample in these reports is probably due to the purity of raw elements Fe and Si. It was reported that the non-doped β-FeSi$_2$ prepared with 4N purity of raw elements exhibited p-type conduction, but the non-doped sample prepared with 5N purity exhibited n-type [59]. In addition, at low-temperature regions, there is a transition from n-type to p-type. For example, as shown in the inset of Fig. 6 (a), the sign of S of $x = 0.05$ changes from negative (-2 μVK^{-1}) to positive ($+1$ μVK^{-1}) as temperature increases from 145 K to 150 K, respectively. This indicates that the conduction of Fe$_{1-x}$Mn$_x$Si$_2$ is dominated by both electrons and holes, where their ratios change with temperatures [48].

The S of all Mn-doped samples is more uniform with temperature, especially at high temperatures, due to the reduction of bipolar effect when the n_H is improved. The highest S value of 456 μVK^{-1} at 245 K is obtained in $x = 0.04$. It then decreases to 380 μVK^{-1} as temperature increases up to 460 K. This tendency suggests that the bipolar effect remains for $x \leq 0.04$ samples. In addition, for $0 \leq x \leq 0.04$, the increase in S at the low-temperature side and suppression of S at the high-temperature side is due to effective mass (m^*) with suppression of n_H. As illustrated in Fig. 6 (b), the increase in S with increasing x for $0 \leq x \leq 0.04$ is because of the increase in m^*. On the other hand, for $0.05 \leq x \leq 0.09$, the decrease in S with increasing x is due to the increase in n_H. The relationship between S, m^*, and n_H can be understood from Mott's formula [60]:
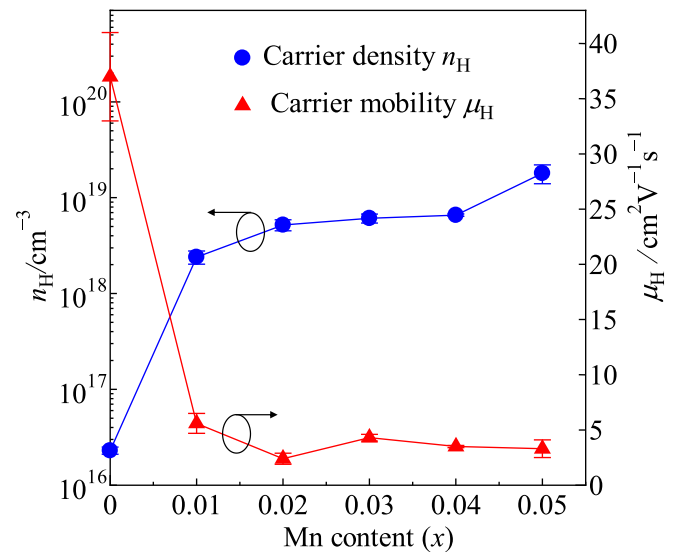

Fig. 4. Room temperature data of carrier density (n_H) plotted with the left axis and carrier mobility (μ_H) plotted with the right axis for Fe$_{1-x}$Mn$_x$Si$_2$ ($0 \leq x \leq 0.05$).

Table 2
Room temperature data of Lorenz number (L_0), scattering factor ($r = -1/2$ for acoustic phonon scattering, carrier density (n_H), mobility (μ_H), Seebeck coefficient (S), electrical resistivity (ρ), total thermal conductivity (κ) for Fe$_{1-x}$Mn$_x$Si$_2$ ($0 \leq x \leq 0.05$).

x	L_0 [V^{2}K^{-2}]	r	n_H [cm^{-3}]	μ_H [cm^{2}V^{-1}s^{-1}]	S [μVK^{-1}]	ρ [Ωcm]	κ [Wm^{-1}K^{-1}]
0	1.792×10^{-8}	$-1/2$	$2.3(2) \times 10^{16}$	37(4)	-127	7.10	7.67
0.01	1.625×10^{-8}	$-1/2$	$2.4(3) \times 10^{18}$	5.6(9)	332	0.45	9.4
0.02	1.626×10^{-8}	$-1/2$	$5.2(6) \times 10^{18}$	2.4(5)	320	0.50	7.9
0.03	1.625×10^{-8}	$-1/2$	$6.1(5) \times 10^{18}$	4.3(3)	345	0.24	7.3
0.04	1.624×10^{-8}	$-1/2$	$6.5(1) \times 10^{18}$	3.5(1)	439	0.27	8.7
0.05	1.631×10^{-8}	$-1/2$	$1.8(4) \times 10^{19}$	3.3(8)	254	0.10	7.2
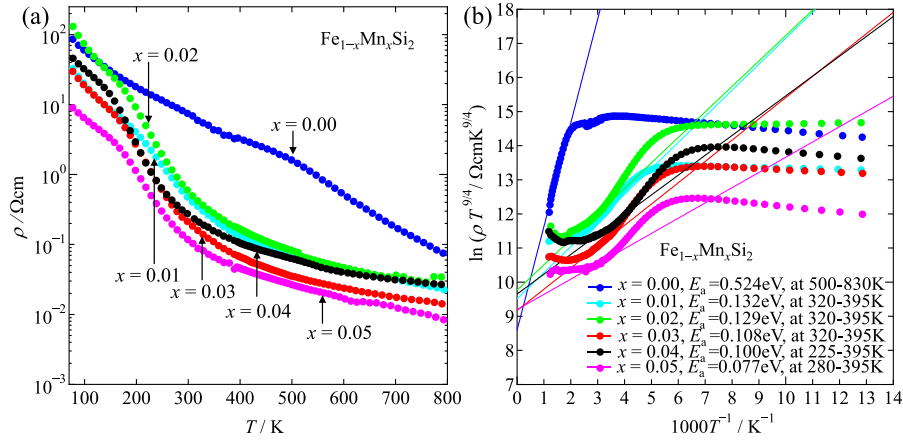
Fig. 5. (a) Temperature dependence of electrical resistivity (ρ) for $Fe_{1-x}Mn_xSi_2$ ($0 \leq x \leq 0.05$). (b) Arrhenius plot of $\ln(\rho T^{9/4})$ versus the reciprocal absolute temperature, where the activation energy (E_a) is estimated from the slope of the straight lines.
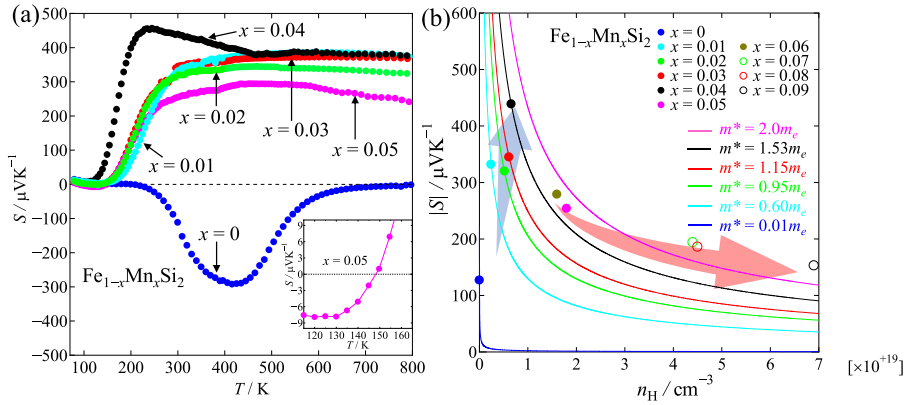
Fig. 6. (a) Temperature dependence of Seebeck coefficient (S) for $Fe_{1-x}Mn_xSi_2$ ($0 \leq x \leq 0.05$). The inset shows the transition of conduction properties from n-type to p-type of $x = 0.05$ at low-temperature region. (b) Absolute Seebeck coefficient $|S|$ versus carrier density (n_H) at room temperature. The solid line is the calculated data from Equation (10) using various effective masses, $m^* = xm_e$, where x is the variables and m_e is the static mass of electrons equal to 9.10938×10^{-31} kg. The data of $|S|$ for $0.06 \leq x \leq 0.09$ at room temperature are taken from our previous work [31]. The shaded blue arrow indicates the region where m^* contributes to the increase in $|S|$ up to $x = 0.04$. The shaded red arrow indicates the region where the n_H contributes to the decrease in $|S|$.

$$|S| = \frac{\pi^2 k_B^2 T}{3|e|\hbar^2} \frac{1}{D(E_F)} \left[\frac{\partial D(E)}{\partial E} \right]_{E=E_F} = \frac{\pi^2 k_B^2 T}{3|e|\hbar^2} \frac{1}{D(E_F)} \frac{\partial D(E_F)}{\partial E_F} \tag{6}$$

Where k_B is Boltzmann constant, T is temperature, e is elementary charge, $\hbar$ is Plack's constant, E_F is the Fermi energy, and $D(E_F)$ is the density of state at Fermi energy. From the Free Electron theory, $D(E_F)$ in the volume (V) is defined by Ref. [51]:

$$D(E_F) = \frac{V}{2\pi^2} \left(\frac{2m^*}{\hbar^2} \right)^{3/2} \sqrt{E_F}$$

$$\implies \frac{\partial D(E_F)}{\partial E_F} = \frac{V}{2\pi^2} \left(\frac{2m^*}{\hbar^2} \right)^{3/2} \frac{\partial(\sqrt{E_F})}{\partial E_F} = \frac{V}{2\pi^2} \left(\frac{2m^*}{\hbar^2} \right)^{3/2} \frac{1}{2} \frac{\sqrt{E_F}}{E_F} = \frac{1}{2E_F} D(E_F) \tag{7}$$

By substituting Equation (7) into (6), we obtain:

$$|S| = \frac{\pi^2 k_B^2 T}{6|e|E_F} \tag{8}$$

The Fermi energy, E_F, is defined by Ref. [51]:

$$E_F = \frac{\hbar^2}{2m^*} (3\pi^2 \times n)^{2/3} \tag{9}$$

By substituting Equation (9) into (8), the relationship between S, m^*, and n_H can be finally obtained as follows:

$$|S| = \frac{k_B^2 T}{3|e|\hbar^2} m^* \left(\frac{\pi}{3n_H} \right)^{2/3} \tag{10}$$

From Equation (10), the $|S|$ is contributed by m^* and n_H. We use this equation to evaluate the m^* by fitting experimental data of $|S|$ with the calculated data as a function of n_H as shown in Fig. 6 (b). Therefore, the increase in m^* contributes to the increase in $|S|$ for $0 \leq x \leq 0.04$, but the increase in n_H contributes to the decrease in $|S|$ for $0.05 \leq x \leq 0.09$. A large increase in m^* with a low amount of Mn doping and almost constant at high Mn doping levels are consistent with the result of carrier mobility as discussed above. In addition, since the m^* is inversely proportional to the curvature of band structure (d^2E/dk^2) as can be expressed by: $m^* = \hbar^2(d^2E/dk^2)^{-1}$, the increase in m^* with the increasing amount of Mn doping suggests that the curvature of the valence band is decreasing [61]. In other words, the curvature of the band structure of β-$FeSi_2$ [53] should become flatter when doping with Mn.

Fig. 7 illustrates the temperature-dependent power factor, $PF=S^2/\rho$, for $Fe_{1-x}Mn_xSi_2$ ($0 \leq x \leq 0.05$). The inset shows that the maximum PF value of the non-doped sample is 3.4 $\mu Wm^{-1}K^{-2}$ at 450 K, but it decreases to about 0 $\mu Wm^{-1}K^{-2}$ as temperature increases to 800K. The
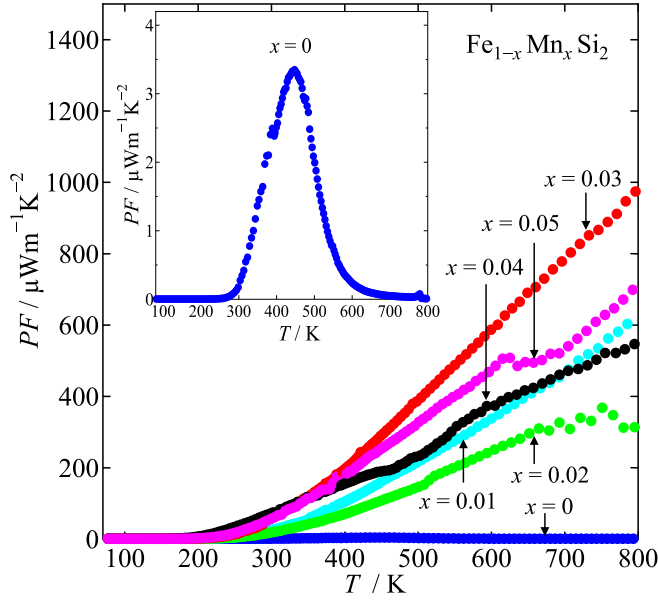
Fig. 7. Temperature dependence of power factor ($PF=S^2/\rho$) for $Fe_{1-x}Mn_xSi_2$ ($0 \leq x \leq 0.05$). The inset magnifies the data of the non-doped sample.

decrease in *PF* of the non-doped sample at high temperatures is provoked by the reduction in $|S|$ due to the bipolar effect. The *PF* values of $0.01 \leq x \leq 0.05$ samples are much higher than that of the $x = 0$ sample due to the decrease in ρ and improvement in *S*. As a result, the maximum *PF* of 970 $\mu Wm^{-1}K^{-2}$ at 800 K is obtained at optimum doping $x = 0.03$. Such *PF* value is higher than the Co-doped sample ($PF = 900$ $\mu Wm^{-1}K^{-2}$) investigated by the previous study [40]. This is because the amount of β-phase (95 % up) in the Mn-doped sample is higher than the β-phase (91 %) in the Co-doped sample, leading to the enhancement of the *S* and *PF*. Therefore, the stability of the β-phase is essential to improve the *PF* values.

The temperature dependence of total thermal conductivity ($\kappa_{\text{total}} = \kappa_l + \kappa_e$) and the electronic part (κ_e) are illustrated in Fig. 8. At below 600K, the κ_{total} of all samples decreases increasing temperature indicating semiconducting behaviors. In contrast, at high temperatures above 600K, the κ_{total} increases with temperature because of the bipolar
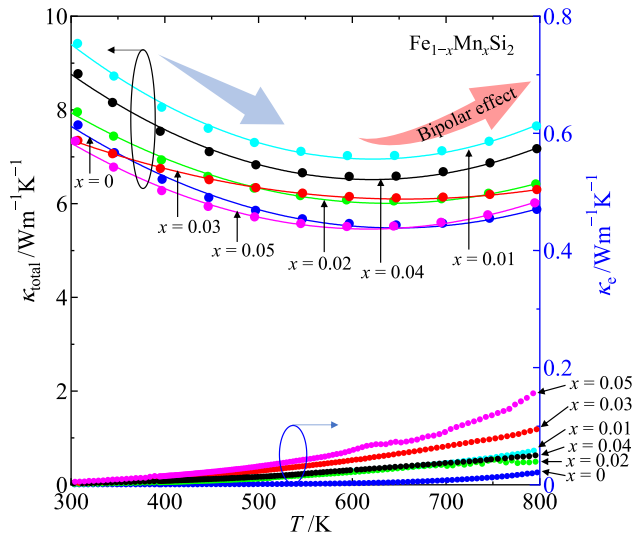
Fig. 8. Temperature dependence of total thermal conductivity (κ_{total}) plotted with the left axis and electronic thermal conductivity ($\kappa_e = L_0T/\rho$) plotted with the right axis for $Fe_{1-x}Mn_xSi_2$ ($0 \leq x \leq 0.05$).

diffusion effect. In addition, the κ_{total} slightly increases with x probably due to the increase in κ_e. The values of κ_e are evaluated by Wiedemann–Franz law: $\kappa_e = L_0T/\rho$, where L_0 is Lorenz number, T is temperature, and ρ is electrical resistivity. In the case of acoustic phonon scattering (scattering factor $r = -1/2$), L_0 is defined by Ref. [62]:

$$L_0 = \left(\frac{k_B}{e}\right)^2 \left[\frac{\left(r+\frac{7}{2}\right)F_{r+\frac{5}{2}}(\eta)}{\left(r+\frac{3}{2}\right)F_{r+\frac{1}{2}}(\eta)} - \left\{ \frac{\left(r+\frac{5}{2}\right)F_{r+\frac{3}{2}}(\eta)}{\left(r+\frac{3}{2}\right)F_{r+\frac{1}{2}}(\eta)} \right\}^2 \right] \quad (11)$$

where $F_n(\eta) = \int_0^\infty \frac{\chi^n}{1+e^{\chi-\eta}}d\chi$, $\chi = \frac{E}{k_BT}$, $\eta = \frac{E_F}{k_BT}$, and E_F is the Fermi energy. The relationship between η and the Seebeck coefficient, *S*, is expressed by:

$$S = \pm\frac{k_B}{e}\left(2\frac{F_1(\eta)}{F_0(\eta)} - \eta\right) \quad (12)$$

From Equation (12), η can be determined by fitting the experimental value of *S* at room temperature. Thus, L_0 can be consequently evaluated from Equation (11) and the data are summarized in Table 2. As illustrated in Fig. 8, the κ_e of all samples monotonically increases with temperature and it also increases with x because of the decrease in ρ. However, the ratio of κ_e to κ_{total} is very small compared to that of κ_l to κ_{total}. This indicates that κ_l has a major contribution to the κ_{total}. Therefore, it is suggested that additional doping with heavy elements such as ruthenium (Ru) or germanium (Ge) could help to reduce the phonon mean free path (l), resulting in a decrease in κ_l and improved TE performance. The relationship between κ_l and l can be expressed by Ref. [50]:

$$\kappa_l = \frac{1}{3}C_V v_G l \quad (13)$$

Where C_V is the specific heat at constant volume, v_G is the phonons group velocity and $l = v_G\tau$; τ is phonon relaxation time. Equation (13) implies that κ_l is proportional to l. Heavy dopants usually introduce significant mass differences compared to the host lattice, resulting in increasing phonon scattering. Thus, the phonon scattering reduces the mean free path or relaxation time, thereby decreasing κ_l.

Fig. 9 shows the temperature dependence of TE performance (*ZT* values) evaluated by Equation (1). As illustrated in the inset, the maximum *ZT* of $x = 0$ is about 2.4×10^{-4} at 450 K and it remarkably decreases as temperature increases. The decrease in *ZT* of $x = 0$ at high temperatures is because of the reduction in *S*, where the bipolar effect dominates. The *ZT* values of $0.01 \leq x \leq 0.05$ samples are much higher than that of the $x = 0$ sample due to improvement in *PF* values, whereas ρ is reduced and *S* is uniform at high temperatures (reduction in bipolar effect). The β-phase stability also contributes to maintaining *S* and improving *ZT*. As a result, the highest *ZT* of 0.12 at 800 K is obtained in optimum doping of $x = 0.03$. Comparing the *ZT* values of samples fabricated by the same method, the *ZT* of the current Mn-doped sample (*ZT* = 0.12) is lower than the *ZT* of our double doping (Ni + Co)-doped sample (*ZT* = 0.31) [39], but relatively higher than the *ZT* of our Co-doped sample (*ZT* = 0.099) [26]. The *ZT* of the Mn-doped sample is lower than that of the (Ni + Co)-doped sample because the effective mass of holes is lighter than that of electrons due to the difference in curvature (d^2E/dk^2) between the bottom of the conduction band and the top of the valence band. The maximum *ZT* of our study is similar to previous reports of Mn-doped samples prepared by the pressure-less sintering method (*ZT* = 0.14) [63], sintering gas-atomized powders using the hot pressing method (*ZT* = 0.1) [64], spray drying and sintering techniques method (*ZT* = 0.15) [65], but is relatively higher than the sample pulse plasma sintering method (*ZT* = 0.06) [34]. However, our proposed direct arc melting method is less time-consuming compared to the pressure sintering method.
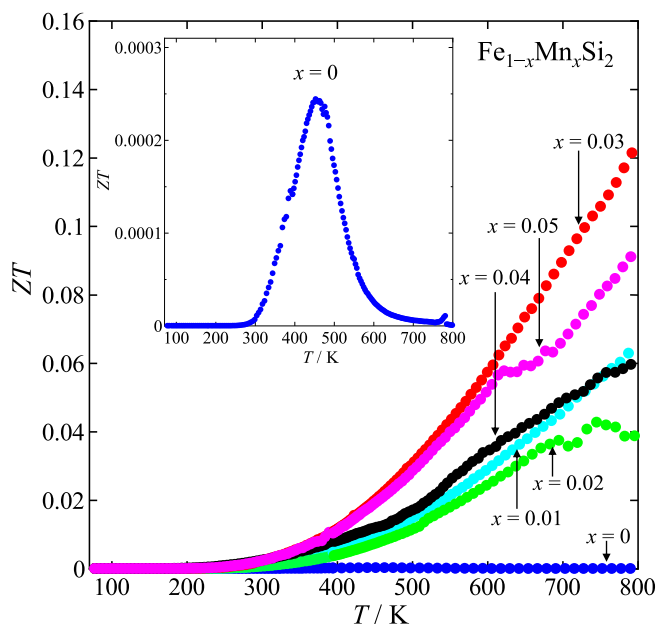
Fig. 9. Temperature dependence of *ZT* values ($ZT = S^2 \rho^{-1} \kappa^{-1} T$) for Fe$_{1-x}Mn_xSi_2$ ($0 \leq x \leq 0.05$). The inset magnifies the data of the non-doped sample.

4. Conclusion

Arc melting and heat treatment processes were used to prepare β-Fe$_{1-x}$Mn$_x$Si$_2$ ($0 \leq x \leq 0.05$) thermoelectric. We found that the semiconducting phase (β-FeSi$_2$) of all samples is higher than 95 % and stable with *x* from 0 to 0.05, while the metallic phases (α-Fe$_2$Si$_5$ and ε-FeSi) share the occupation with only less than 5 %. The β-phase in Mn-doped samples is more stable than other metal-doped samples such as Co and Ni. The addition of Mn improves the carrier density but decreases mobility. However, electrical transport significantly improves due to the increase in carrier density. The Seebeck coefficient is enhanced and stable at high temperatures due to the reduction of the bipolar effect and β-phase stability. The thermal conductivity slightly increases with Mn doping. Consequently, the maximum power factor of 970 μWm^{-1}K^{-2} and *ZT* of 0.12 at 800 K are obtained in a 3 % Mn-doped sample. Our study offers a comprehensive analysis on the correlation between phase contents, electrical transport, and thermoelectric properties, which could be useful in the field of thermoelectric research.

CRediT authorship contribution statement

Sopheap Sam: Writing – review & editing, Writing – original draft, Visualization, Validation, Formal analysis, Data curation, Conceptualization. **Umar Farooq:** Methodology. **Rio Oshita:** Investigation. **Hiroshi Nakatsugawa:** Supervision, Software, Resources, Project administration, Funding acquisition.

Declaration of competing interest

The authors declare that they have no known competing financial interests or personal relationships that could have appeared to influence the work reported in this paper.

Data availability

No data was used for the research described in the article.

References

[1] X.F. Zheng, C.X. Liu, Y.Y. Yan, Q. Wang, A review of thermoelectrics research – recent developments and potentials for sustainable and renewable energy applications, Renew. Sustain. Energy Rev. 32 (2014) 486–503, https://doi.org/10.1016/j.rser.2013.12.053.

[2] X.-L. Shi, J. Zou, Z.-G. Chen, Advanced thermoelectric design: from materials and structures to devices, Chem. Rev. 120 (2020) 7399–7515, https://doi.org/10.1021/acs.chemrev.0c00026.

[3] R. Sok, J. Kusaka, Development and validation of thermal performances in a novel thermoelectric generator model for automotive waste heat recovery systems, Int. J. Heat Mass Tran. 202 (2023) 123718, https://doi.org/10.1016/j.ijheatmasstransfer.2022.123718.

[4] R. Sok, J. Kusaka, Experimental and modeling analysis on thermoelectric heat recovery to maximize the performance of next-generation diesel engines dedicated for future electrified powertrains, Appl. Therm. Eng. 219 (2023) 119530, https://doi.org/10.1016/j.applthermaleng.2022.119530.

[5] A. Nozariasbmarz, R.A. Kishore, W. Li, Y. Zhang, L. Zheng, M. Sanghadasa, B. Poudel, S. Priya, Thermoelectric coolers for high-power-density 3D electronics heat management, Appl. Phys. Lett. 120 (2022) 3–8, https://doi.org/10.1063/5.0088129.

[6] Y. Zhang, B. Ge, J. Feng, N. Kuang, H. Ye, Z. Yuan, M. Wu, B. Jiang, J. Li, Q. Sun, L. Niu, M. Zhu, Y. Xu, W. Jie, R. Liu, S. Dong, C. Zhou, High-performance self-powered flexible thermoelectric device for accelerated wound healing, Adv. Funct. Mater. 2403990 (2024) 1–8, https://doi.org/10.1002/adfm.202403990.

[7] H.J. Goldsmid, Theory of thermoelectric refrigeration and generation, in: H. Robert, J. Chennupati, K. Yoshiyuki, M.O. Richard, P. Jürgen, S. Tae-Yeon, U. Shin-ichi, M.W. Zhiming (Eds.), Intoduction to Thermoelectr, second ed., Springer Berlin Heidelberg, Berlin, Heidelberg, 2016, pp. 9–24, https://doi.org/10.1007/978-3-662-49256-7_2.

[8] K. Hasezaki, A. Yamada, H. Tsukuda, M. Araoka, Thermoelectric properties of Bi-Te module prepared by mechanical alloying, Mater. Trans., JIM 37 (1996) 1224–1227, https://doi.org/10.2320/matertrans1989.37.1224.

[9] Y. Xiao, L.-D. Zhao, Charge and phonon transport in PbTe-based thermoelectric materials, NPJ Quantum Mater. 3 (2018) 55, https://doi.org/10.1038/s41535-018-0127-y.

[10] S. Sam, L.A. Gan Lim, S. Thirumalai, A. Wiranata, Jamasri, J. Sentanuhady, G.N. C. Santos, M.A. Muflikhun, Novel lead–tin telluride (PbSnTe) thermoelectric material manufactured via horizontal vapour phase growth technique (HVPG), Manuf. Lett. 40 (2024) 11–15, https://doi.org/10.1016/j.mfglet.2024.01.002.

[11] H. Nakatsugawa, M. Saito, Y. Okamoto, High-temperature thermoelectric properties of perovskite-type Pr$_{0.9}$Sr$_{0.1}$Mn$_{1-x}$Fe$_x$O$_3$ ($0 \leq x \leq 1$), J. Electron. Mater. 46 (2017) 3262–3272, https://doi.org/10.1007/s11664-017-5366-3.

[12] H. Fukutomi, Y. Konno, K. Okayasu, M. Hasegawa, H. Nakatsugawa, Texture development of Ca$_3$Co$_4$O$_9$ thermoelectric oxide by high temperature plastic deformation and its contribution to the improvement in electric conductivity, Mater. Sci. Eng. 527 (2009) 61–64, https://doi.org/10.1016/j.msea.2009.08.012.

[13] H. Ohta, Thin film growth and thermoelectric properties of electron conducting oxides, J. Ceram. Soc. Japan. 130 (2022) 22061, https://doi.org/10.2109/jcersj2.22061.

[14] H. Nakatsugawa, Y. Kamatani, Y. Okamoto, C.H. Hervoches, Crystal structure, magnetism, and thermoelectric properties of Nd$_{1-x}$Sr$_x$FeO$_{3-\delta}$ ($0.1 \leq x \leq 0.9$), Jpn. J. Appl. Phys. 62 (2023) 043001, https://doi.org/10.35848/1347-4065/acc9f3.

[15] Y. Zhang, H. Ohta, Recent progress in thermoelectric layered cobalt oxide thin films, NPG Asia Mater. 15 (2023) 67, https://doi.org/10.1038/s41427-023-00520-w.

[16] X.-Q. Chen, S.-J. Fan, C. Han, T. Wu, L.-J. Wang, W. Jiang, W. Dai, J.-P. Yang, Multiscale architectures boosting thermoelectric performance of copper sulfide compound, Rare Met. 40 (2021) 2017–2025, https://doi.org/10.1007/s12598-020-01698-6.

[17] X. Chen, H. Zhang, Y. Zhao, W.-D. Liu, W. Dai, T. Wu, X. Lu, C. Wu, W. Luo, Y. Fan, L. Wang, W. Jiang, Z.-G. Chen, J. Yang, Carbon-encapsulated copper sulfide leading to enhanced thermoelectric properties, ACS Appl. Mater. Interfaces 11 (2019) 22457–22463, https://doi.org/10.1021/acsami.9b06212.

[18] O. Caballero-Calero, J.R. Ares, M. Martín-González, Environmentally friendly thermoelectric materials: high performance from inorganic components with low toxicity and abundance in the earth, Adv. Sustain. Syst. 5 (2021) 2100095, https://doi.org/10.1002/adsu.202100095.

[19] S. Katsuyama, H. Matsushima, M. Ito, Effect of substitution for Ni by Co and/or Cu on the thermoelectric properties of half-Heusler ZrNiSn, J. Alloys Compd. 385 (2004) 232–237, https://doi.org/10.1016/j.jallcom.2004.02.061.

[20] H. Nakatsugawa, T. Ozaki, H. Kishimura, Y. Okamoto, Thermoelectric properties of heusler Fe$_2$TiSn alloys, J. Electron. Mater. 49 (2020) 2802–2812, https://doi.org/10.1007/s11664-019-07855-7.

[21] A. Difalco, I.G. Winning, M. Palumbo, M. Baricco, A. Castellero, E. Alleno, Transport properties of Co$_2$HfSn Heusler alloy obtained by rapid solidification and

sintering, Solid State Sci. 149 (2024) 107455, https://doi.org/10.1016/j.solidstatesciences.2024.107455.

[22] A. Nozariasbmarz, A. Agarwal, Z.A. Coutant, M.J. Hall, J. Liu, R. Liu, A. Malhotra, P. Norouzzadeh, M.C. Öztürk, V.P. Ramesh, Y. Sargolzaeiaval, F. Suarez, D. Vashaee, Thermoelectric silicides: a review, Jpn. J. Appl. Phys. 56 (2017) 05DA04, https://doi.org/10.7567/JJAP.56.05DA04.

[23] A.T. Burkov, Silicide thermoelectrics: materials for energy harvesting, Phys. Status Solidi 215 (2018) 1800105, https://doi.org/10.1002/pssa.201800105.

[24] L. Abbassi, D. Mesguich, D. Berthebaud, S. Le Tonquesse, B. Srinivasan, T. Mori, L. Coulomb, G. Chevallier, C. Estournès, E. Flahaut, R. Viennois, M. Beaudhuin, Effect of nanostructuring on the thermoelectric properties of β-FeSi$_2$, Nanomaterials 11 (2021) 2852, https://doi.org/10.3390/nano11112852.

[25] G. Kim, H. Shin, J. Lee, W. Lee, A review on silicide-based materials: thermoelectric and mechanical properties, Met. Mater. Int. 27 (2021) 2205–2219, https://doi.org/10.1007/s12540-020-00609-9.

[26] S. Sam, H. Nakatsugawa, Y. Okamoto, Optimization of Co additive amount to improve thermoelectric properties of β-FeSi$_2$, Jpn. J. Appl. Phys. 61 (2022) 111002, https://doi.org/10.35848/1347-4065/ac96b7.

[27] P. Qiu, J. Cheng, J. Chai, X. Du, X. Xia, C. Ming, C. Zhu, J. Yang, Y. Sun, F. Xu, X. Shi, L. Chen, Exceptionally heavy doping boosts the performance of iron silicide for refractory thermoelectrics, Adv. Energy Mater. 12 (2022) 2200247, https://doi.org/10.1002/aenm.202200247.

[28] S. Sam, S. Odagawa, H. Nakatsugawa, Y. Okamoto, Effect of Ni substitution on thermoelectric properties of bulk β-Fe$_{1-x}$Ni$_x$Si$_2$ (0 ≤ x ≤ 0.03), Materials 16 (2023) 927, https://doi.org/10.3390/ma16030927.

[29] T. Saito, R. Asakawa, Production of (Fe,Co)Si$_2$ and (Fe.Mn)Si$_2$ thermoelectric materials by spark plasma sintering, Crystals 14 (2023) 56, https://doi.org/10.3390/cryst14010056.

[30] J. Cheng, L. Gan, J. Zhang, J. Xi, L. Xi, J. Yang, T. Deng, P. Qiu, X. Shi, L. Chen, Thermoelectric properties of heavily Co-doped β-FeSi$_2$, J. Mater. Sci. Technol. 187 (2024) 248–257, https://doi.org/10.1016/j.jmst.2023.11.039.

[31] S. Sam, U. Farooq, M. Namba, K. Yamazaki, H. Nakatsugawa, Structure relations with transport properties in p-type thermoelectric materials: iron silicides, J. Alloys Compd. 989 (2024) 174367, https://doi.org/10.1016/j.jallcom.2024.174367.

[32] M. Shibuya, M. Kawata, Y. Shinohara, M. Ohyanagi, Eco-fabrication process and thermoelectric properties of β-FeSi$_2$, Trans. Mater. Res. Soc. Japan. 40 (2015) 219–222, https://doi.org/10.14723/tmrsj.40.219.

[33] H. Inoue, T. Kobayashi, M. Kato, S. Yoneda, A low-cost production method of FeSi$_2$ power generation thermoelectric modules, J. Electron. Mater. 45 (2016) 1767–1771, https://doi.org/10.1007/s11664-015-4208-4.

[34] F. Dąbrowski, Ł. Ciupiński, J. Zdunek, J. Kruszewski, R. Zybała, A. Michalski, K. Jan Kurzydłowski, Microstructure and thermoelectric properties of p and n type doped β-FeSi$_2$ fabricated by mechanical alloying and pulse plasma sintering, Mater. Today Proc. 8 (2019) 531–539, https://doi.org/10.1016/j.matpr.2019.02.050.

[35] X. Qu, S. Lü, J. Hu, Q. Meng, Microstructure and thermoelectric properties of β-FeSi$_2$ ceramics fabricated by hot-pressing and spark plasma sintering, J. Alloys Compd. 509 (2011) 10217–10221, https://doi.org/10.1016/j.jallcom.2011.08.070.

[36] X. Du, P. Hu, T. Mao, Q. Song, P. Qiu, X. Shi, L. Chen, Ru alloying induced enhanced thermoelectric performance in FeSi$_2$-based compounds, ACS Appl. Mater. Interfaces 11 (2019) 32151–32158, https://doi.org/10.1021/acsami.9b10648.

[37] H.Y. Chen, X.B. Zhao, T.J. Zhu, Y.F. Lu, H.L. Ni, E. Müller, A. Mrotzek, Influence of nitrogenizing and Al-doping on microstructures and thermoelectric properties of iron disilicide materials, Intermetallics 13 (2005) 704–709, https://doi.org/10.1016/j.intermet.2004.12.019.

[38] X. Du, P. Qiu, J. Chai, T. Mao, P. Hu, J. Yang, Y.-Y. Sun, X. Shi, L. Chen, Doubled thermoelectric figure of merit in p-type β-FeSi$_2$ via synergistically optimizing electrical and thermal transports, ACS Appl. Mater. Interfaces 12 (2020) 12901–12909, https://doi.org/10.1021/acsami.0c00321.

[39] S. Sam, H. Nakatsugawa, Y. Okamoto, Improved thermoelectric performance of Co-doped β-FeSi$_2$ by Ni substitution, Mater. Adv. 4 (2023) 2821–2830, https://doi.org/10.1039/D3MA00153A.

[40] S. Sam, K. Yamazaki, H. Nakatsugawa, Investigation of phase fraction in α-Fe$_2$Si$_5$, ε-FeSi, and β-FeSi$_2$ thermoelectric materials doped with Co and Ni, Solid State Commun. 371 (2023) 115287, https://doi.org/10.1016/j.ssc.2023.115287.

[41] X.B. Zhao, H.Y. Chen, E. Müller, C. Drasar, Thermoelectric properties of Mn doped FeSi$_x$ alloys hot-pressed from nitrided rapidly solidified powders, Appl. Phys. A 80 (2005) 1123–1127, https://doi.org/10.1007/s00339-004-2596-z.

[42] M. Ohtaki, D. Ogura, K. Eguchi, H. Arai, Thermoelectric properties of sintered FeSi$_2$ with microstructural modification, Chem. Lett. 22 (1993) 1067–1070, https://doi.org/10.1246/cl.1993.1067.

[43] L. Pauling, A.M. Soldate, The nature of the bonds in the iron silicide, FeSi, and related crystals, Acta Crystallogr. 1 (1948) 212–216, https://doi.org/10.1107/S0365110X48000570.

[44] B.C. Sales, E.C. Jones, B.C. Chakoumakos, J.A. Fernandez-Baca, H.E. Harmon, J.W. Sharp, E.H. Volckmann, Magnetic, transport, and structural properties of Fe$_{1-x}$Ir$_x$Si, Phys. Rev. B 50 (1994) 8207–8213, https://doi.org/10.1103/PhysRevB.50.8207.

[45] G. Li, W. Bai, N. Shi, Q. Fang, M. Xiong, J. Yang, Z. Ma, H. Rong, Linzhiite, FeSi$_2$, a redefined and revalidated new mineral species from Luobusha, Tibet, China, Eur. J. Mineral 24 (2012) 1047–1052, https://doi.org/10.1127/0935-1221/2012/0024-2237.

[46] J. Tani, H. Kido, Mechanism of electrical conduction of Mn-doped β-FeSi$_2$, J. Appl. Phys. 86 (1999) 464–467, https://doi.org/10.1063/1.370753.

[47] J.J. Gong, A.J. Hong, J. Shuai, L. Li, Z.B. Yan, Z.F. Ren, J.-M. Liu, Investigation of the bipolar effect in the thermoelectric material CaMg$_2$Bi$_2$ using a first-principles study, Phys. Chem. Chem. Phys. 18 (2016) 16566–16574, https://doi.org/10.1039/C6CP02057G.

[48] J. Tani, H. Kido, Electrical properties of Co-doped and Ni-doped β-FeSi$_2$, J. Appl. Phys. 84 (1998) 1408–1411, https://doi.org/10.1063/1.368174.

[49] J. Tani, H. Kido, Thermoelectric properties of β-Fe$_{1-x}$Co$_x$Si$_2$ semiconductors, Jpn. J. Appl. Phys. 40 (2001) 3236, https://doi.org/10.1143/JJAP.40.3236.

[50] T. Takeuchi, New thermoelectric materials with precisely determined electronic structure and phonon dispersion, in: D.M. Rowe (Ed.), Thermoelectr. Its Energy Harvest., first ed., Taylor & Francis Group, Abingdon, UK, 2017 https://doi.org/10.1201/b11891, 7-1-7–27.

[51] C. Kittel, Introduction to Solid State Physics, Wiley, New York, 1986.

[52] C.T. Sah, Fundamentals of Solid-State Electronics, World Scientific, Singapore, 1991.

[53] S.J. Clark, H.M. Al-Allak, S. Brand, R.A. Abram, Structure and electronic properties of FeSi$_2$, Phys. Rev. B 58 (1998) 10389–10393, https://doi.org/10.1103/PhysRevB.58.10389.

[54] S. Sen, D. Acharya, P.K. Guha, P. Banerji, P. Pramanik, Comprehensive electrical characterization and theoretical analysis of Mn and as doped β-FeSi$_2$ through DFT: a promise to rectification and photovoltaic applications, J. Appl. Phys. 134 (2023) 025702, https://doi.org/10.1063/5.0149138.

[55] U. Birkholz, J. Schelm, Mechanism of electrical conduction in β-FeSi$_2$, Phys. Status Solidi 27 (1968) 413–425, https://doi.org/10.1002/pssb.19680270141.

[56] J.-H. Bahk, A. Shakouri, Enhancing the thermoelectric figure of merit through the reduction of bipolar thermal conductivity with heterostructure barriers, Appl. Phys. Lett. 105 (2014) 052106, https://doi.org/10.1063/1.4892653.

[57] M. Ito, H. Nagai, T. Tahata, S. Katsuyama, K. Majima, Effects of Zr substitution on phase transformation and thermoelectric properties of β-FeSi$_2$, J. Appl. Phys. 92 (2002) 3217–3222, https://doi.org/10.1063/1.1502202.

[58] M. Ito, H. Nagai, E. Oda, S. Katsuyama, K. Majima, Effects of P doping on the thermoelectric properties of β-FeSi$_2$, J. Appl. Phys. 91 (2002) 2138–2142, https://doi.org/10.1063/1.1436302.

[59] Y. Isoda, H. Udono, Preparation and thermoelectric properties of iron disilicide, in: D.M. Rowe (Ed.), Thermoelectr. Its Energy Harvest., first ed., CRC Press, 2012 https://doi.org/10.1201/b11891, 18-1–18–25.

[60] N.F. Mott, Conduction in glasses containing transition metal ions, J. Non-Cryst. Solids 1 (1968) 1–17, https://doi.org/10.1016/0022-3093(68)90002-1.

[61] J. Piprek, Electron energy bands, in: Semicond. Optoelectron. Devices, Elsevier, 2003, pp. 13–48, https://doi.org/10.1016/B978-0-08-046978-2.50027-2.

[62] L.-D. Zhao, S.-H. Lo, J. He, H. Li, K. Biswas, J. Androulakis, C.-I. Wu, T.P. Hogan, D.-Y. Chung, V.P. Dravid, M.G. Kanatzidis, High performance thermoelectrics from earth-abundant materials: enhanced figure of merit in PbS by second phase nanostructures, J. Am. Chem. Soc. 133 (2011) 20476–20487, https://doi.org/10.1021/ja208658w.

[63] M. Ito, H. Nagai, T. Tanaka, S. Katsuyama, K. Majima, Thermoelectric performance of n-type and p-type β-FeSi$_2$ prepared by pressureless sintering with Cu addition, J. Alloys Compd. 319 (2001) 303–311, https://doi.org/10.1016/S0925-8388(01)00920-3.

[64] Y. Kimura, Y. Yamada, Y.W. Chai, Thermoelectric properties of nearly single-phase β-FeSi$_2$ alloys fabricated by gas-atomized powder sintering, Mater. Trans. 60 (2019) 652–661, https://doi.org/10.2320/matertrans.MB201805.

[65] O. Yamashita, S. Tomiyoshi, N. Sadatomi, Thermoelectric properties of p- and n-type FeSi$_2$ prepared by spray drying, compaction and sintering technique, J. Mater. Sci. 38 (2003) 1623–1629, https://doi.org/10.1023/A:1023251004461.